

www.acsnano.org

Role of Femtosecond Pulsed Laser-Induced Atomic Redistribution in Bimetallic Au-Pd Nanorods on Optoelectronic and Catalytic **Properties**

Mohammadreza Nazemi, Sajanlal R. Panikkanvalappil, Chih-Kai Liao, Mahmoud A. Mahmoud, and Mostafa A. El-Sayed*



Downloaded via GEORGIA INST OF TECHNOLOGY on May 25, 2021 at 16:38:29 (UTC). See https://pubs.acs.org/sharingguidelines for options on how to legitimately share published articles.

Cite This: https://doi.org/10.1021/acsnano.1c02347



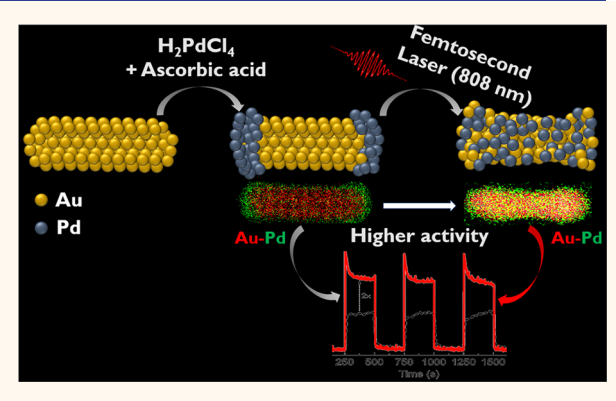
ACCESS

III Metrics & More

Article Recommendations

Supporting Information

ABSTRACT: Utilizing solar energy for chemical transformations has attracted a growing interest in promoting the clean and modular chemical synthesis approach and addressing the limitations of conventional thermocatalytic systems. Under light irradiation, noble metal nanoparticles, particularly those characterized by localized surface plasmon resonance, commonly known as plasmonic nanoparticles, generate a strong electromagnetic field, excited hot carriers, and photothermal heating. Plasmonic nanoparticles enabling efficient absorption of light in the visible range have moderate catalytic activities. However, the catalytic performance of a plasmonic nanoparticle can be significantly enhanced by incorporating a highly catalytically active metal domain onto its surface. In this study, we demonstrate that femtosecond laser-induced atomic



redistribution of metal domains in bimetallic Au-Pd nanorods (NRs) can enhance its photocurrent response by 2-fold compared to parent Au-Pd NRs. We induce structure changes on Au-Pd NRs by irradiating them with a femtosecond pulsed laser at 808 nm to precisely redistribute Pd atoms on AuNR surfaces, resulting in modified electronic and optical properties and, thereby, enhanced catalytic activity. We also investigate the trade-off between the effect of light absorption and catalytic activity by optimizing the structure and composition of bimetallic Au-Pd nanoparticles. This work provides insight into the design of hybrid plasmonic-catalytic nanostructures with well-tailored geometry, composition, and structure for solar-fuelbased applications.

KEYWORDS: plasmonic photoelectrochemistry, photoelectrocatalysis, plasmonic—catalytic nanoparticle, bimetallic nanorods, femtosecond pulsed laser

INTRODUCTION

Solar energy is abundant, accessible, and open-source, meeting the world's growing energy demands. The sun supplies $\sim 10^4$ times the annual global energy consumption. Even with energy demand projected to double in the upcoming decades, solar energy is still a viable option. 1,2 Photoelectrochemical (PEC) cells enable the conversion of solar energy to storable and transportable fuels and could address the existing challenge of mismatch between renewable energy supply and demand.³⁻⁷ Understanding the electronic and thermal properties of metal nanoparticles and their interactions with other materials is imperative to improve PEC cells' efficiency.

Noble metal nanoparticles are known to support coherent oscillatory modes of their conduction band electrons when

photoexcited with a resonant frequency, producing localized surface plasmon resonances (LSPR).8-11 Resonant electromagnetic fields can couple with these modes resulting in photon absorption and/or scattering and the generation of intense electromagnetic surface near-fields, which can enhance a range of optical and electronic processes such as fluorescence, ¹² Raman scattering, ^{13,14} Förster resonance

Received: March 18, 2021 Accepted: May 24, 2021



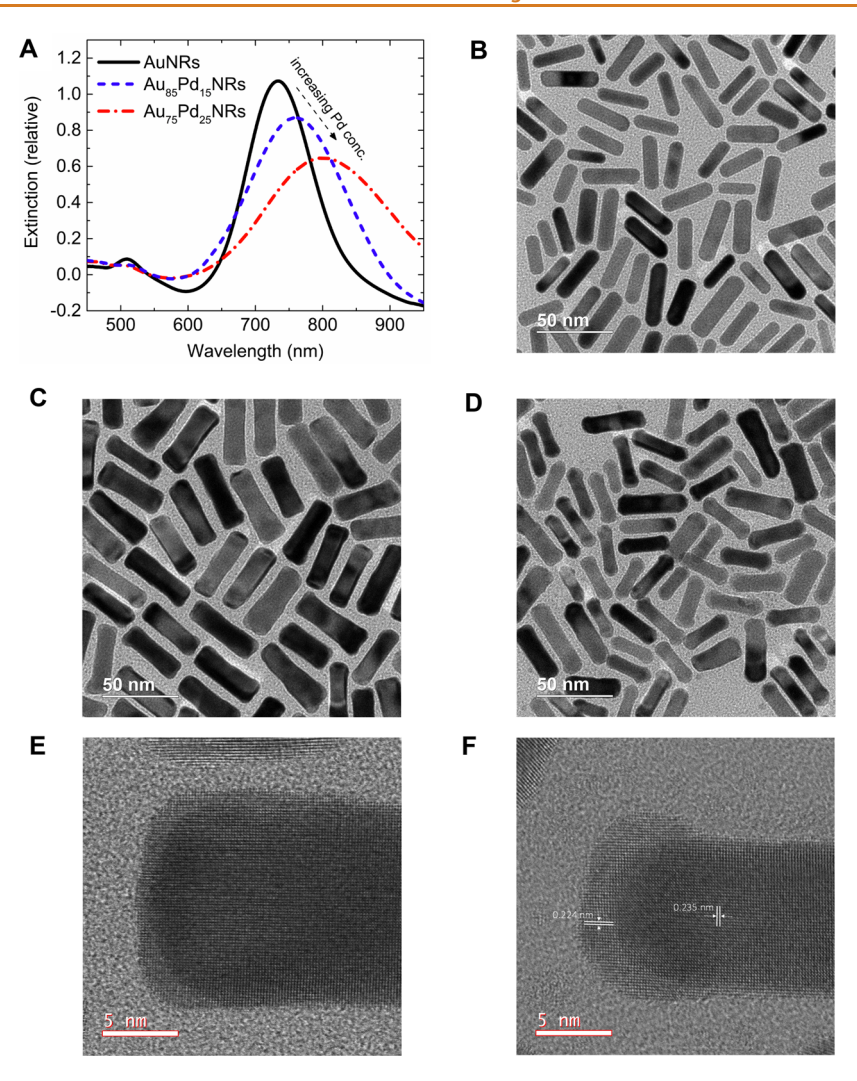


Figure 1. (A) UV-vis extinction spectra of AuNRs and Au-Pd NRs with different Pd concentrations. As Pd concentration increases, the LSPR peak redshifts and the plasmonic intensity for both longitudinal and transverse plasmon modes dampens. TEM images of (B) AuNRs, (C) Au₈₅Pd₁₅NRs (Pd content: 15% at.), (D) Au₇₅Pd₂₅NRs (Pd content: 25% at.). HRTEM images of (E) Au₈₅Pd₁₅NRs and (F) Au₇₅Pd₂₅NRs.

energy transfer (FRET),¹⁵ and resonant energy transfer between metallic and semiconducting nanoparticles.¹⁶ The LSPR can be excited by UV, visible, or near-infrared (NIR) light, which depends on the nanoparticle's size, shape, composition, structure (hollow or solid), and the dielectric function of the surrounding medium.^{17–19} By placing various plasmonic nanoparticles in their proximity (<10 nm), a strong electromagnetic field is generated at a certain distance due to the coupling of the electromagnetic field of individual plasmonic nanoparticles.²⁰ The contribution of absorption and scattering to the extinction spectra of plasmonic nanoparticles is calculated by finite-difference time-domain (FDTD) or discrete-dipole approximation (DDA).^{21,22}

PECs typically consist of architecturally sophisticated photoelectrocatalysts assembled into a structure designed to optimize light harvesting and catalytic chemical transformations. Physical and chemical processes critical to PEC cells' operation occur at the electrode–electrolyte interface. ^{23–26} After plasmonic excitation of metal nanoparticles with incident light, the plasmon can quickly dephase through electron–surface scattering on the time scale of a few femtoseconds (fs), generating nonthermal hot electrons. After a few hundred fs,

electron-electron scattering produces a distribution of electrons with temperature on the order of hundreds of degrees above the surrounding medium.27 Within a few picoseconds (ps) of the initial excitation, the absorbed energy is transferred to the nanoparticle's lattice via electron-phonon coupling (τ_{e-ph}) . The final stage of heat dissipation to the surrounding medium by thermal conduction occurs on a longer time scale ranging from several tens of ps to 10 ns through phonon-phonon coupling (τ_{ph-ph}) . At this stage, the heated nanoparticle lattice transfers heat to the surrounding medium, resulting in increasing the medium's temperature until the nanoparticle lattice and its surrounding medium reach equilibrium temperature, which is higher than the temperature of the bulk medium. Before nonthermal hot electrons lose energy to the surrounding medium, they can excite electronic or vibrational transitions in adsorbed molecules on the nanoparticle's surface, thus enabling photocatalytic reactions.²⁸⁻³⁴

Despite various design strategies for enhancing the catalytic activity of plasmonic nanocatalysts, including controlling nanocatalysts' size and shape, they have exhibited moderate activity for driving photochemical reactions. Incorporating a

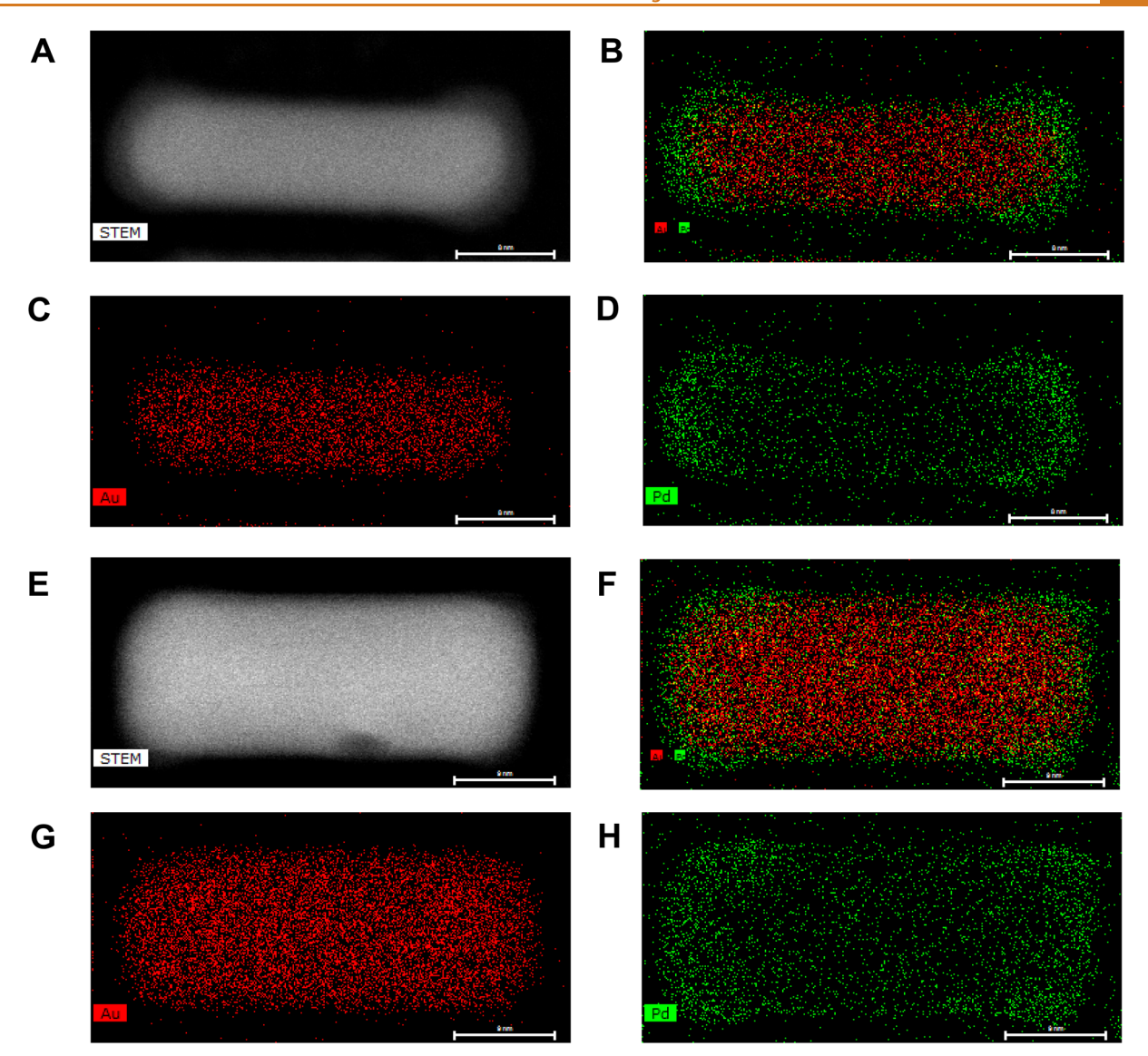


Figure 2. STEM (A) and EDX elemental mapping (B, C, D) of a representative single Au₇₅Pd₂₅NR. STEM (E) and EDX elemental mapping (F, G, H) of a representative single Au₈₅Pd₁₅NR.

cocatalyst made of transition metal nanoparticles could improve the photocatalytic activity in the hybrid plasmonic—catalytic nanoparticles. 35,36 In this hybrid system, a plasmonic nanoparticle is mainly responsible for absorbing light and generating hot carriers while transition metal catalytic reactors handle the chemical reactions. 37,38 In addition, passivating highly unstable crystal facets of nanomaterials by a selective overgrowth of a second metal can significantly improve the nanocatalyst's colloidal stability and durability during photoelectrochemical reactions. This is essential for preserving catalytic activity under harsh experimental conditions and their potential translation in industrial catalysis.

Mechanistic understanding of heat dissipation dynamics in the nanoparticles during plasmon excitation through their interface and subsequent nanoparticle melting, which takes place at the fs time scale, enables manipulation of the structure, leading to the discovery of plasmonic nanostructures with modified optical, electrical, and catalytic properties.^{39–42} The exposure of plasmonic nanostructures with a fs pulsed laser can result in thermalization. If strong enough, it can induce structural changes in the nanoparticle itself, including melting/

reshaping, ejection from a substrate, and fragmentation into smaller particles. 43-46 As atomic distribution in a hybrid nanoparticle plays a significant role in its catalytic performance, fs pulsed laser irradiation can likely modify the catalytically active surface area by redistribution of atomic species within hybrid nanoparticles.⁴⁷ There are two common mechanisms associated with reshaping, fragmentation, and atomic redistribution of metal nanoparticles (NPs) upon pulsed laser irradiation: (1) the Coulomb explosion and (2) photothermal surface evaporation (ablation). $^{48-51}$ Both mechanisms can occur depending upon the laser pulse duration (τ_p) , laser energy, and optical and thermophysical properties of nanoparticles. In the Coulomb explosion, the electron temperature (T_e) should be high enough (>7000 K) to enable thermionic electron emission using a high-energy pulsed laser. The ejection of electrons from the nanoparticle surface is followed by the spontaneous fission of charged metallic clusters due to the charge repulsion. The photothermal ablation happens by transferring thermal energy to the lattice until the lattice temperature (T_L) exceeds the boiling point of the NPs. ^{52,53} In addition, a near-field ablation mechanism was used to interpret

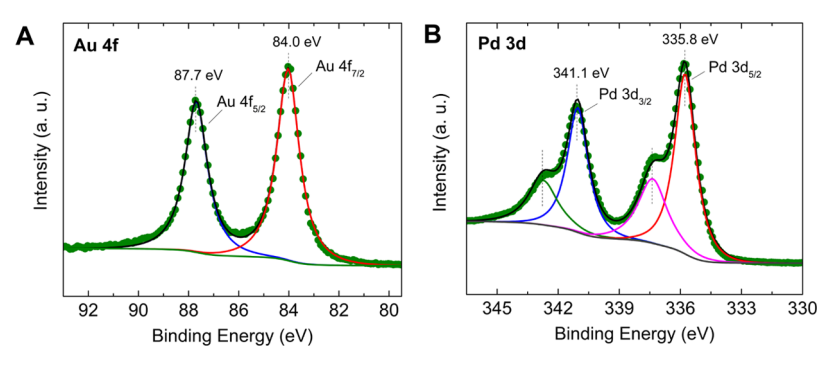


Figure 3. XPS spectra of (A) Au 4f and (B) Pd 3d of bimetallic Au-Pd NRs. All spectra were shift corrected using a standard reference C 1s, C-C peak at 284.8 eV.

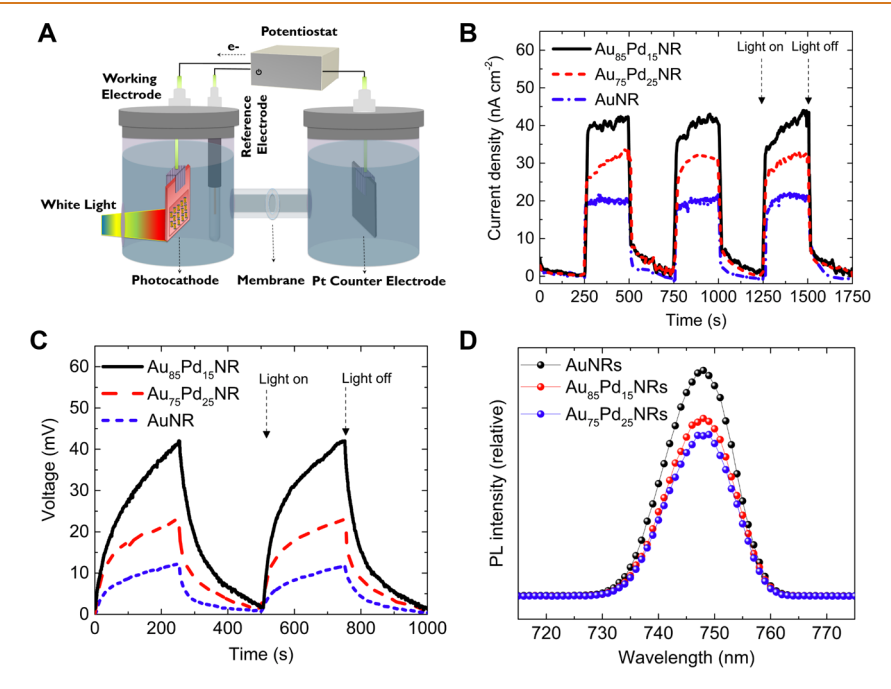


Figure 4. (A) Schematic of the photoelectrochemical setup. (B) Transient photocurrent response of AuNRs and bimetallic Au–Pd NRs in N_2 -saturated electrolyte (0.5 M LiClO₄ (aq)) under 1 sun illumination. Photocurrent data are collected at the open circuit potential of the cell. (C) Transient photovoltage response of AuNRs and AuPdNRs in N_2 -saturated electrolyte (0.5 M LiClO₄ (aq)) under 1 sun illumination. (D) PL spectra of AuNRs and bimetallic Au–Pd NRs with two different concentrations.

the spallation of solid fragments from the surface of plasmonic nanoparticles exposed to an intense laser field. The nanoparticles' plasmon field enhances the laser field at the hotspot on their surface, inducing the reshaping or fragmentation of such spots. ⁵¹

In our previous study, we demonstrated that Au nanorods (AuNRs) exhibited the highest catalytic activity for nitrogen reduction reaction (NRR) compared to those of solid Au nanocubes (AuNCs) and nanospheres (AuNSs).²⁸ This is due to the two plasmon peaks (i.e., transverse and longitudinal modes) achieved for AuNRs, which promote light absorption compared with the one plasmon peak of AuNCs or AuNSs with the same operating conditions.²⁸ In addition, the higher absorption cross-section, extinction coefficient, and visible to NIR light responsiveness of AuNRs have made them ideal candidates for applications where localized heat delivery is advantageous (e.g., plasmonic photothermal therapy of cancer cells). 54,35 Here, we demonstrate how the structure and atomic redistribution, as well as charge carrier dynamics at interfaces in hybrid plasmonic-catalytic nanoparticles affect PEC cells' performance. We also investigate the role of Pd content in

modulating the light absorption capability of a plasmonic antenna to enhance its catalytic activity.

RESULTS AND DISCUSSION

AuNRs with two LSPR peaks, corresponding to the transverse (510 nm) and longitudinal (735 nm) modes, are synthesized by the modified seed-mediated method (Figure 1A). 56 AuNRs have a length of 37 \pm 4.5 nm and a width of 9.5 \pm 0.5 nm, as obtained from transmission electron microscopy (TEM) images (Figure 1B). Bimetallic Au-Pd NRs with various concentrations are synthesized by regioselective reduction of palladium salt on the AuNR surface at 40 °C using ascorbic acid. Reduction of Pd²⁺ for 5 h resulted in the growth of a \sim 1.5 nm thick Pd shell on the AuNRs while the longitudinal plasmon mode redshifts from 735 to 760 nm (Figure 1A and C). The LSPR bands broaden due to the increased dephasing of the plasmon at the Au-Pd interface (Figure 1A). Increasing the reaction time allowed for the reduction of Pd²⁺ resulting in the growth of a larger Pd shell at the tip of the AuNRs (\sim 2.5 nm) and further redshifting in the LSPR peak to 800 nm

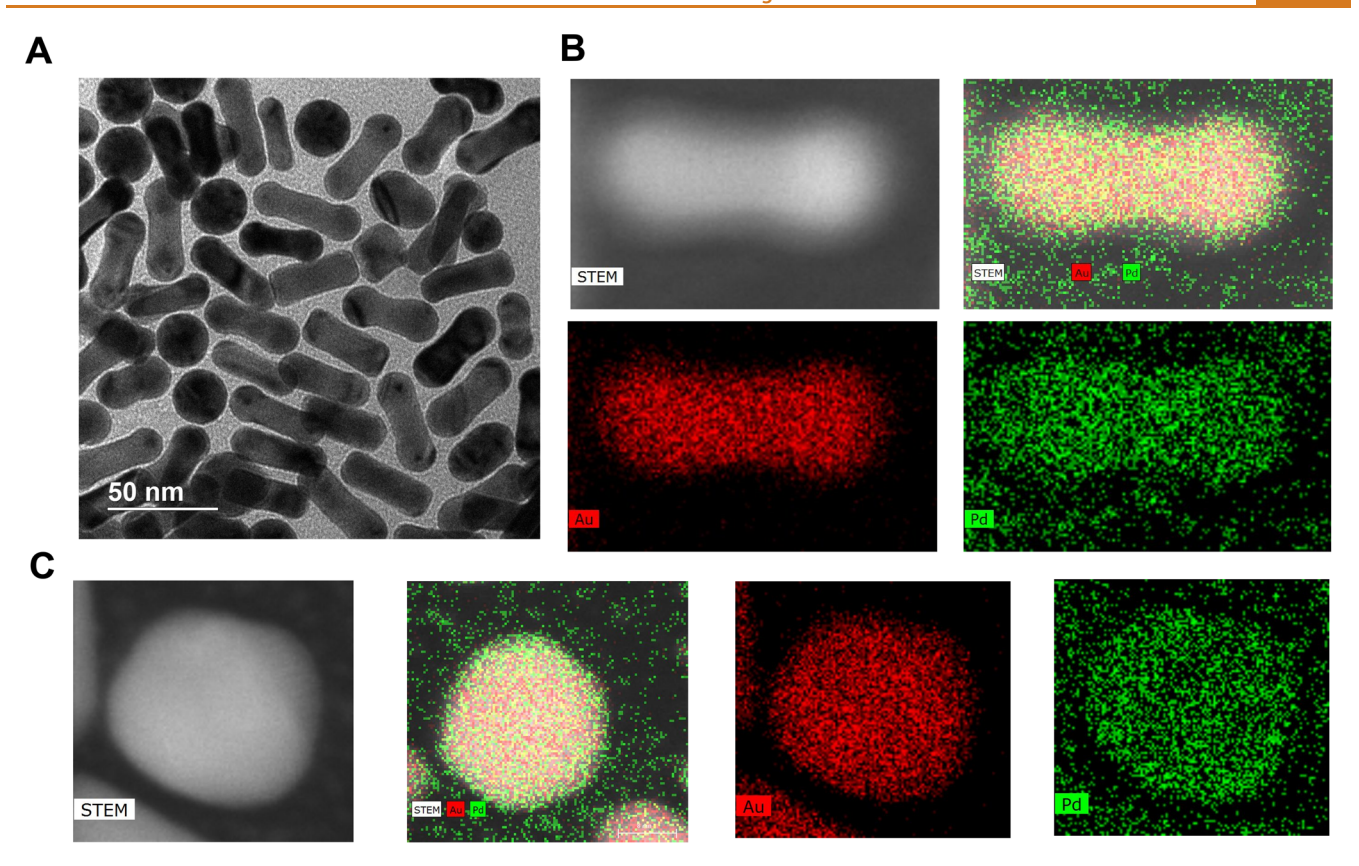


Figure 5. (A) TEM image of Au₈₅Pd₁₅NRs after fs pulsed laser irradiation. (B, C) EDX elemental mappings of dumbbell and sphere shapes of resulting Au₈₅Pd₁₅NRs after 1 h of fs pulsed laser irradiation (200 mW, 808 nm).

(Figures 1A and D and S1). The Au and Pd content for each nanoparticle is provided in Table S1, representing bimetallic Au-Pd NRs which contained an atomic ratio of 15% Pd and 85% Au (Au₈₅Pd₁₅NRs) and 25% Pd and 75% Au (Au₇₅Pd₂₅NRs) as determined by inductively coupled plasma emission spectroscopy (ICPES). By increasing the Pd content, the absorption intensity dampens for 15% and 25% Pd content due to the plasmon quenching by Pd atoms (Figure 1A). Highresolution transmission electron microscopy (HRTEM) reveals lattice spacings of 0.235 and 0.224 nm corresponding to the (111) lattice plane of the face-centered cubic (FCC) structure Au and Pd (Figure 1E and F). The presence of Pd on the body of AuNRs with a thickness of ~0.25 nm is evident (Figure S2). Scanning transmission electron microscopy (STEM) and energy dispersive X-ray (EDX) spectroscopy were used to ascertain the structure, the elemental composition, and the distribution of bimetallic Au-Pd NRs (Figures 2A-H and S3). It is observed that, for both Au-Pd NRs, Pd accumulation is higher at the tip than the body of the NRs.

X-ray photoelectron spectroscopy (XPS) results of bimetallic Au–Pd NRs exhibit a doublet for Au 4f at 84.0 and 87.7 eV. This implies that the zero-valence state of Au (Au⁰) is maintained after adding and reducing the Pd²⁺ precursor in bimetallic Au–Pd NRs (Figure 3A).⁵⁷ The Pd 3d spectrum reveals two pairs of doublets. The doublet peaks at 335.8 and 341.1 eV are attributed to Pd at a zero-valence state, while the doublet peaks with lower intensities than those of zero-valence Pd metal located at 337.4 and 342.8 eV are ascribed to Pd at the oxidized states (Pdⁿ⁺) (Figure 3B).⁵⁸ The X-ray diffraction (XRD) pattern of bimetallic Au–Pd NRs reveals three

pronounced peaks for Pd at higher 2θ angles (40.4° , 46.8° , 68.2°) compared to that of Au peaks (38.2° , 44.5° , 64.7°), corresponding to the (111), (200), and (220) index facets (Figure S4). The Pd peaks appear at higher 2θ angles due to the smaller lattice parameter (3.890 Å) of Pd than that of Au (4.079 Å).

PEC measurements are performed in a standard threeelectrode setup in N2-saturated electrolyte (0.5 M LiClO4 (aq)) using photocathodes comprised of nanoparticles (AuNRs, Au₈₅Pd₁₅NRs, Au₇₅Pd₂₅NRs) supported on indium tin oxide (ITO) (Figure 4A). The electrolyte is under constant N₂ bubbling and magnetic stirring. The external light source is illuminated through a quartz window with a 1-in. diameter located on the cell's front side (Figure 4A). A 300 W Xe light source generates the air mass (AM) 1.5-irradiance with the power intensity of 100 mW cm⁻². A standard Si-solar cell is used to calibrate the illumination intensity near the sample surface, and the distance is fixed to 6 cm to obtain 1 sun illumination. Higher photocurrent densities are obtained after depositing Pd on AuNRs as Pd catalytic sites serve as trapping centers for hot electrons generated by AuNRs, retarding electron-hole recombination (Figure 4B).

Increasing the Pd content from 15% to 25% results in decreasing the photocurrent response due to the decrease in light absorption of $Au_{75}Pd_{25}NRs$ (plasmon quenching by Pd atoms) compared to that of $Au_{85}Pd_{15}NRs$ (Figure 4B). This also indicates an enhanced charge separation and transfer process at the interface using the $Au_{85}Pd_{15}NR$ photocathode. The same trend is observed for photovoltage, indicating that suppressing recombination boosts both the photocurrent and the photovoltage of the cell (Figure 4C). Photoluminescence

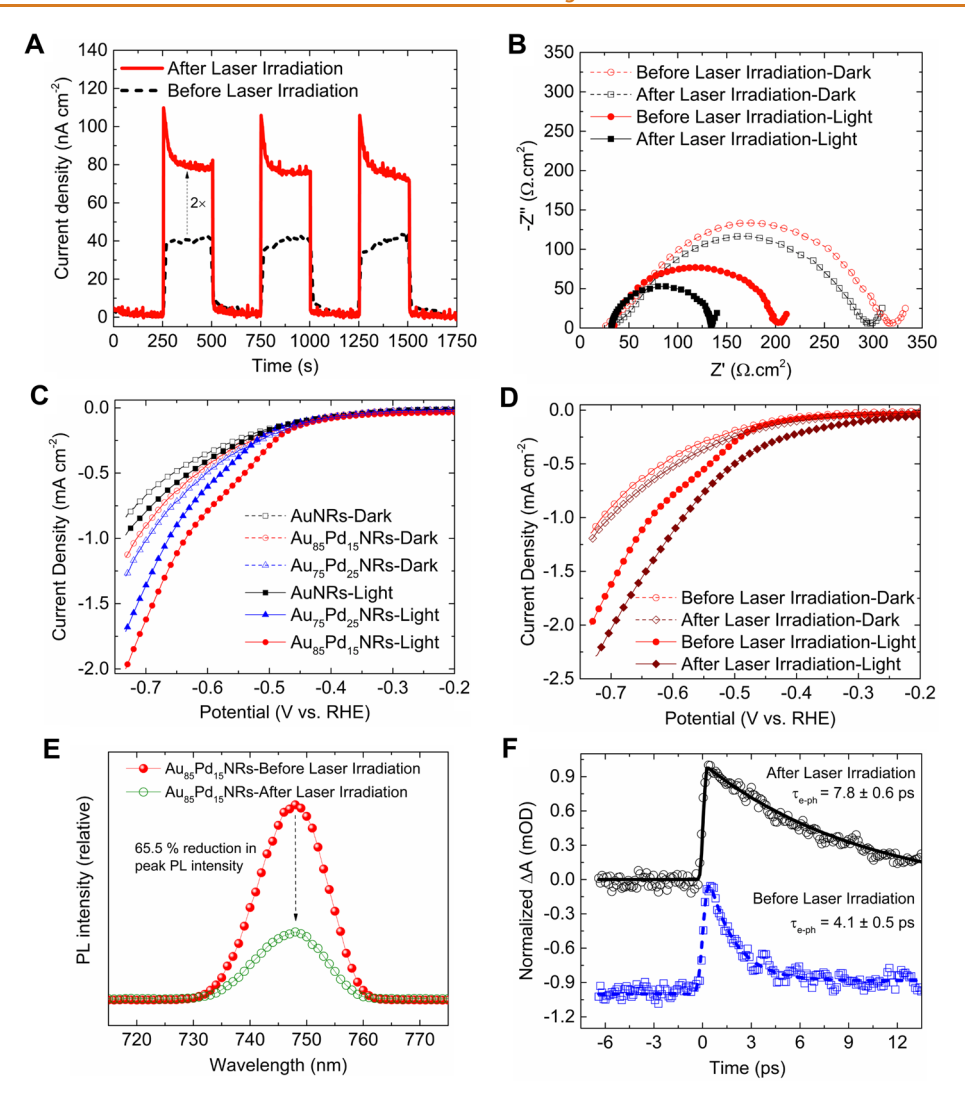


Figure 6. (A) Transient photocurrent response of $Au_{85}Pd_{15}NRs$ before and after surface modification via fs laser irradiation (200 mW, 808 nm). (B) Nyquist plots of $Au_{85}Pd_{15}NRs$ before and after laser-induced reshaping under photoirradiation and dark conditions at an applied bias of 0.5 V (vs Ag/AgCl) in 0.5 M LiClO₄ (aq) electrolyte. The equivalent circuit model consists of charge transfer resistance (R_{CT}), ohmic resistance (R_{S}), and double layer capacitance (C_{DL}). R_{CT} was obtained from the diameter of semicircles for each photoelectrocatalyst. (C) LSV of various photoelectrocatalysts under dark and light (a 300 W Xe light source provides the air mass (AM) 1.5-irradiance with the power intensity of 100 mW cm⁻²) conditions. (D) LSV of $Au_{85}Pd_{15}NRs$ before and after laser-induced reshaping under dark and light conditions. (E) PL spectra of $Au_{85}Pd_{15}NRs$ before and after fs laser irradiation. The peak PL intensity drops 65.5% using structurally modified $Au_{85}Pd_{15}NRs$ after fs laser irradiation, suggesting more effective quenching of hot carriers by Pd sites. (F) Kinetic traces from the TA spectra for plasmon bleach recovery of $Au_{85}Pd_{15}NRs$ before and after fs laser irradiation pumped at 405 nm and probed at 510 nm for tranverse surface plasmon absorption of nanoparticles. The black solid and blue dashed lines are fits with decay times of 4.1 \pm 0.5 and 7.8 \pm 0.6 ps for electron—phonon coupling times (τ_{e-ph}).

(PL) measurements are carried out to investigate the charge transfer for various photocathodes studied in this work. The emissions data are collected using 375 nm excitation wavelength (Figure 4D). The main PL peak at 748 nm approximately coincides with the longitudinal surface plasmon resonance of AuNRs. ^{59,60} The emission intensity decreases after Pd addition and after increasing Pd content, suggesting the fluorescence quenching by Pd, further proving photogenerated charge transfer from Au to Pd. This is also consistent with the absorption data, where increasing Pd content results in decreasing light absorption intensity.

Since $Au_{85}Pd_{15}NRs$ showed the best PEC performance, they are selected to be further evaluated for structural reorganization under fs pulsed laser irradiation. We conducted time-dependent experiments to explore Pd redistribution on the

AuNR surface as well as the shape and morphological changes of nanoparticles upon exposure to the fs laser. The laser beam's fundamental output (3.6 mJ, 40 fs pulse duration, 1000 Hz pulse frequency) centered at 808 nm is used to conduct the experiments. Although the laser excitation wavelength is not located at the LSPR peak of $Au_{85}Pd_{15}NRs$ (760 nm), it is close enough (78.5%) to tangibly induce structural changes and atomic redistribution on bimetallic Au-Pd NRs. It is noted that the laser excitation wavelength overlaps well with the LSPR peak of $Au_{75}Pd_{25}NRs$ (800 nm). The extinction spectra of nanoparticles were monitored as a function of exposure time. The plasmon intensity slightly dampens, which might be attributed to the Pd redistribution (Figure S5). The LSPR peak slightly blue shifts due to the changes in the geometry, including the conversion of rods to spheres and changes in the

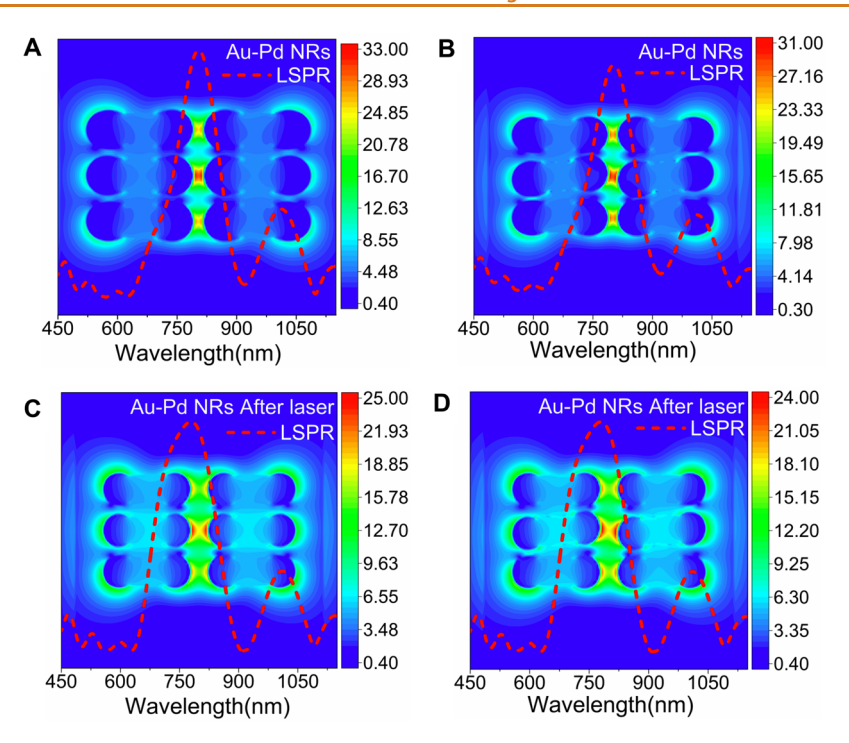


Figure 7. LSPR spectra and plasmon field intensity and distribution of (A, C) six aligned Au-Pd NRs and (B, D) six unaligned Au-Pd NRs before and after fs pulsed laser irradiation, respectively.

aspect ratio and Pd atom redistribution on the AuNR surface (Figures 5A, S5, and S6). The majority of Au₈₅Pd₁₅NRs preserved their shape with a slight shape change from rods to the dumbbell shape. The EDX elemental mappings and STEM images reveal that Pd atoms with an approximate size of 1.5-2 nm are uniformly distributed on the AuNR surface after 1 h fs pulsed laser irradiation for both dumbbell and sphere shapes (Figures 5B and C and S7). In addition, the distinct XRD peaks for Au and Pd are observed after laser irradiation, ruling out the possibility of the alloy formation (Figure S4). The cross-sectional line profiles on single dumbbell- and sphereshaped nanoparticles after laser irradiation confirm the Au core and thin Pd shell (Figure S8). In our fs pulsed laser excitation of bimetallic Au–Pd NRs in which the plasmon field intensity is high at the tips of the rods, and there is no sign of Au-Pd alloying, the photothermal-near-field ablation hybrid mechanism is the likely mechanism for atomic redistribution of Pd on the AuNR surface. ⁵¹ In addition, as the condition $\tau_{\rm p} < \tau_{\rm e-ph} \ll$ $\tau_{\rm ph-ph}$ is satisfied in our experiments, the Coulomb explosion might also affect the atomic redistribution of Pd on the AuNR surface, as the laser energy is sufficient to increase T_e to exceed the fragmentation temperature whereas T_L might not surpass the boiling point of the Au-Pd NPs. 52,53,6

A 2-fold enhancement in photocurrent density is obtained after pulsed laser irradiation of bimetallic Au–Pd NRs, indicating facile interface charge kinetics after the structural reorganization of Pd on the AuNR surface (Figure 6A). Furthermore, electrochemical impedance spectroscopy (EIS) is performed under dark and light conditions to obtain Nyquist plots (Figure 6B). The charge transfer resistance ($R_{\rm CT}$) marginally improved from 291 to 263 Ω ·cm² after Pd atom redistribution on AuNR surfaces under dark conditions. This is because the Au and Pd content before and after laser irradiation remained relatively unchanged. However, a noticeable improvement is observed under illumination (from 167 to 102 Ω .cm²), suggesting an enhanced transfer

of photogenerated charge carriers, promoting efficient photocatalytic reactions. The PEC performances of all nanoparticles studied in this work were compared by measuring current density (under dark and light conditions) vs potential (J-V) plots (Figure 6C). Under the dark condition, a higher current density is achieved after Pd deposition on AuNRs and subsequently by increasing Pd content from 15% to 25%.

This is due to Pd's higher electrochemical surface area than that of Au, providing more active sites for catalytic reactions. 62 However, under 1 sun illumination, Au₈₅Pd₁₅NRs achieved the highest photocurrent density due to the compromise between light absorption of Au and catalytic activity of Pd. At any fixed current density, the difference between the value of potential under dark and light conditions represents the photovoltage, which is also the highest for Au₈₅Pd₁₅NRs. For example, at the fixed current density of 0.75 mA cm⁻², 81.5, 34.7, and 22.3 mV photovoltages are achieved for Au₈₅Pd₁₅NRs, Au₇₅Pd₂₅NRs, and AuNRs. The photovoltage under the same operating conditions $(J = 0.75 \text{ mA cm}^{-2})$ increased to 105.0 mV after laser-induced atomic redistribution of Au₈₅Pd₁₅NRs (Figure 6D). The current density under dark conditions did not change significantly before and after laser irradiation, similar to the Nyquist plot trend. However, the photocurrent density under 1 sun illumination improved tangibly in the wide range of applied negative potentials (i.e., cathodic) using structurally modified Au₈₅Pd₁₅NRs by fs laser (Figure 6D).

To further understand the origin of the enhanced photocurrent density after fs laser irradiation, PL spectra were collected for both rod- and sphere-shaped nanoparticles in Figure 5A. The PL quenching is more intense (65.5% reduction in emission for rods vs 32.5% for spheres) for the rod shape after fs laser irradiation compared to that of the sphere shape (Figures 6E and S9). This indicates that Pd atom redistribution on AuNRs after laser irradiation more effectively lowers the number of hot carriers in the AuNRs available for radiative recombination, resulting in enhanced photocurrent response. In addition, the photocurrent response of AuNRs is almost two times higher than that of AuNSs (Figure S10). This rules out the possibility that an enhanced photocurrent response after fs laser irradiation of Au₈₅Pd₁₅NRs is due to the formation of sphere-type nanoparticles. The formation of sphere-type nanoparticles can be controlled by adjusting the fs laser power intensity and exposure time. It is noted that, through the careful optimization of the mixture of nanoparticles, the photocurrent density can be further improved by extending the extinction spectrum of the mixture of nanoparticles to cover the entire visible region.⁶³ Furthermore, transient absorption measurements reveal that the average lifetime of bimetallic Au–Pd NRs increases (7.8 \pm 0.6 ps) after laser-induced atomic redistribution, indicating the efficient transfer of hot electrons from Au to Pd sites (Figure 6F). The τ_{e-ph} of Au nanoparticles of various shapes (e.g., spheres, rods, cages) ranges from 1–4 ps. 10,64,65

To further understand the enhanced activity of bimetallic Au-Pd NRs after fs pulsed laser irradiation, the XPS Pd 3d and Au 4f spectra were collected. The Pd 3d peaks shift to lower binding energies (0.2 eV), while Au 4f peaks appear at higher binding energies (0.3 eV) after laser irradiation, indicating the stronger interaction and better charge redistribution between Au and Pd and possible electron transfer from Au plasmonic metal to Pd sites in Au₈₅Pd₁₅NRs (Figure S11). In addition, the d-band center $(E - E_f)$ upshifts from -3.66 to -3.39 eV after atomic redistribution of bimetallic Au-Pd NRs, indicating an enhanced binding strength of adsorbed species on the catalyst surface using structurally modified Au₈₅Pd₁₅NRs (Figure S12). It is noted that Pd in bimetallic Au-Pd NRs not only acts as active catalytic sites but also improves the colloidal stability of the nanocatalyst under fs laser irradiation. Cleaned AuNRs destabilize, aggregate, and fall out of the suspension only after 30 min of fs pulsed laser irradiation (90 mW) (Figure \$13). However, the atomically redistributed Au₈₅Pd₁₅NRs through 1 h illumination with fs pulsed laser exhibited a stable photocurrent response with a laser source (808 nm, 200 mW) (Figure S14).

FDTD calculations were conducted to study the optical properties and plasmon field intensity and distribution of bimetallic Au-Pd NRs before and after fs pulsed laser irradiation on the surface of the glass substrate. Pd atoms were distributed on AuNR surfaces (i.e., tip and body) similar to the high-resolution microscopic results (Figures 2 and 5). Pd atoms are primarily located at the AuNR tips before laser irradiation and then partially moved to the body of AuNRs after laser irradiation. The LSPR peak position slights blue shifts after atomic redistribution of Pd atoms from the tip to the body of AuNRs after laser irradiation, agreeing well with the experimentally observed results (Figure 7). In addition, the plasmon field intensity for an array of six (un)aligned Au-Pd NRs decreased after laser irradiation (Figure 7C, D). However, the surface area of the plasmon field is increased using structurally modified Au-Pd NRs. Increasing the plasmon field's extent can positively affect catalytic activity as it is directly proportional to the available hot spots responsible for driving light-driven catalytic reactions. It is noted that the plasmon intensity for a single Au-Pd nanorod and three Au-Pd nanorods increases after laser irradiation (Figure S15). A direct comparison with experiments requires the actual orientation and the number of adjacent Au-Pd nanorods on the substrate during measurements.

We qualitatively evaluated the performance of photoelectrocatalysts in the N₂ and N₂H₄ reduction reaction through ex-situ surface-enhanced Raman spectroscopy (SERS). N₂H₄ was selected in this work to probe the activity of various photocathodes as we have previously demonstrated that N₂H₄ is an intermediate species in NRR for ammonia synthesis. 62,66 In addition, Pd-based catalysts have been shown to interact with N₂ under ambient conditions.^{67,68} The SERS spectra are collected before and after the photoelectrocatalytic reactions under 1 sun illumination at an applied potential of -0.4 V vs RHE for 12 h. In PEC NRR, the peak that appeared at ~2900 cm⁻¹ corresponds to N-H stretching, suggesting the formation of NH₃. This peak intensity is stronger after the reaction and for the photocathode comprised of structurally modified Au₈₅Pd₁₅NRs by fs pulsed laser irradiation, indicating a higher photoelectrocatalytic activity achieved by this photocathode (Figure S16A). In addition, similar experiments were performed by adding 20 μ M of N₂H₄ in the electrolyte. The peak that appeared at $\sim 1144 \text{ cm}^{-1}$ is attributed to the N-N stretching, the specific fingerprint of N₂H₄ present in the electrolyte. A decrease in this peak intensity indicates the consumption of N₂H₄ in the photoelectrocatalytic reaction (Figure S16A). The growth in the intensity of peaks at 2890 and 3222 cm⁻¹ suggests the formation of NH₃ from N₂H₄ (Figure S16B). The intensities of these peaks are stronger after fs laser-induced atomic redistribution of AugsPd₁₅NRs. In addition, the TEM images of the structurally modified bimetallic Au-Pd nanorods before and after the PEC measurements show that the morphology of nanoparticles is maintained after the test (Figure S17).

CONCLUSION

We demonstrated that fs pulsed laser-induced atomic redistribution of Pd in bimetallic Au-Pd nanorods (NRs) resulted in modified optical, electrical, and catalytic properties of hybrid plasmonic-catalytic nanoparticles. The photocurrent response was increased by 2-fold compared to parent Au-Pd NRs using structurally modified Au-Pd NRs. The trade-off between the effect of light absorption and catalytic activity of hybrid NRs was investigated by optimizing the composition of bimetallic Au-Pd nanoparticles. XPS and UPS confirmed an enhanced charge distribution between Au and Pd, and an improved binding strength between adsorbates and the catalyst surface was achieved using structurally modified Au-Pd NRs after fs laser irradiation. An intense PL quenching was observed (65.5% reduction in emission) after fs laser irradiation of nanoparticles, suggesting that redistributed Pd atoms effectively lower the number of hot carriers for radiative recombination. TA measurements reveal that the average $\tau_{\rm e-ph}$ of bimetallic Au–Pd nanorods increases (from 4.1 to 7.8 ps) after pulsed laser irradiation, confirming the efficient transfer of hot electrons to atomically redistributed Pd sites. FDTD calculations revealed that the plasmon field's extent increases after laser-induced atomic redistribution of Pd on AuNR surface, which is beneficial in enhancing the light-driven catalytic reaction's activity. Ex-situ SERS exhibited that an enhanced photoelectrocatalytic activity is achieved in nitrogen reduction reaction and hydrazine reduction reaction using modified bimetallic Au-Pd NRs through fs pulsed laser irradiation. This work provides a scientific framework for the design of hybrid plasmonic-catalytic nanostructures with wellcontrolled geometry, structure, and composition, as well as

modified electronic and catalytic properties for solar-fuel-based applications.

METHODS

Chemicals and Materials. Gold(III) chloride trihydrate (HAuCl₄·3H₂O), sodium borohydride (NaBH₄), cetyltrimethylammonium bromide (CTAB), silver nitrate (AgNO₃), ascorbic acid, palladium(II) chloride (PdCl₂), potassium chloride (KCl), and Nafion solution (5% wt) were purchased from Sigma-Aldrich. Indium tin oxide (ITO) coated one surface (4−8 Ω , Delta Technologies, USA), N₂ (UHP, 100%, Airgas, USA), platinum (100 mesh, 99.9% trace metal basis, Sigma-Aldrich, USA), Ni wire (0.5 mm, ≥99.9% trace metals basis, Sigma-Aldrich), cation exchange membrane (CEM, FKB-PK-130, FuMA-Tech GmbH, Germany), and conductive silver paint (Ted Pella Inc.) were used for experiments.

Synthesis of AuNRs and Bimetallic Au-Pd NRs. AuNRs were synthesized following the method reported in our prior studies. 56,69 The seed nanoparticles required for the nanorod synthesis were prepared by adding 250 μ L of 10 mM HAuCl₄ to 7 mL of 100 mM CTAB followed by 600 µL of 10 mM ice-cold NaBH₄ solution under stirring for 3 min. A growth solution was prepared by adding 4.25 mL of HAuCl₄ (10 mM), 625 μ L of AgNO₃ (10 mM), and 675 μ L of ascorbic acid (100 mM) into 100 mL of 100 mM CTAB solution. Next, 400 μ L of seed solution was added into the 100 mL growth solution, and the resulting solution was kept undisturbed for 8 h at 25 °C. The as-prepared AuNR solution was cleaned by centrifugation at 10 000 rpm for 10 min and was further used for synthesizing bimetallic Au-Pd NRs by following a modified procedure reported earlier. 70 Briefly, 10 mM of H₂PdCl₄ solution was prepared by dissolving PdCl₂ powder in 0.02 M HCl solution. A 0.5 mL portion of 100 mM CTAB was added to 10 mL of the AuNR solution before the reaction. Subsequently, 1 mL of 0.1 M ascorbic acid was added into 10 mL of AuNR suspension, and Pd overgrowth was initiated by the addition of 200 μ L of 10 mM M H₂PdCl₄ into this solution followed by adding 50 μ L of 0.1 M HCl. The resultant solution was kept at 25 °C for 4 h, which yielded Au₈₅Pd₁₅NRs. To obtain Au₇₅Pd₂₅NRs, the aforementioned experiment was conducted for 12 h. Nanoparticles were cleaned by centrifugation at 10 000 rpm for 10 min two times before use in experiments.

Photoelectrochemical Experiments in the Liquid-Phase System. All photoelectrochemical measurements were conducted at 20 °C lab temperature in 0.5 M LiClO₄ (aq) electrolyte in a standard three-electrode setup using various prepared photocathodes comprised of nanoparticles deposited on the ITO substrate as the working electrode, Pt mesh as the counter electrode, and Ag/AgCl reference electrodes (3M, BASi, USA) using a CHI instrument potentiostat (CHI, 760D). The CEM separated the anodic and cathodic compartments. To prepare a photocathode, 300 μ L of nanoparticles with concentrations reported in Table S1 and 1.5 μ L of Nafion solution were sonicated and drop-casted onto a square of ITO (1 cm × 1 cm) and then dried under a N₂ atmosphere at 75 °C for 1 h.

Transient Photocurrent and Photovoltage Measurements. Before starting the photocurrent and photovoltage measurements, N_2 gas was purged through the cell into the 0.5 MLiClO₄ (aq) solution to remove the dissolved oxygen gas for 1 h and purging continued during measurements at the open-circuit potential of the cell. The air mass (AM) 1.5-irradiance with the power intensity of 100 mW cm⁻² is generated using a 300 W Xe light source.

Electrochemical Impedance Spectroscopy. Electrochemical impedance spectroscopy (EIS) data was collected by applying an alternating potential of 5 mV amplitude in the frequency range of 100 kHz to 10^{-2} Hz at an applied bias of 0.5 V (vs Ag/AgCl) in 0.5 M LiClO₄ (aq) solution.

All potentials in this study were *iR*-compensated and reported on the reversible hydrogen electrode (RHE) scale. The Ag/AgCl scale is converted to the RHE scale using the following equation:

$$E_{\text{RHE}} = E_{\text{Ag/AgCl}} + \frac{2.3RT}{F} \text{pH} + E_{\text{Ag/AgCl}}^{\circ}$$
 (1)

where $E_{\rm RHE}$ is the potential on the RHE scale, $E_{\rm Ag/AgCl}^{\circ}=0.2027$ at 20 °C, $E_{\rm Ag/AgCl}$ is the potential vs a Ag/AgCl reference electrode, T is the operating temperature (K), R is the gas constant (8.314 J/mol K), F is the Faraday's constant (C/eq), and the pH of the electrolyte is 8. The electrolyte is saturated with N₂ gas for 1 h prior to the measurement at the flow rate of 20 mL/min.

Instrumentation. TEM imaging was performed using a Hitachi HT7700 TEM with an acceleration voltage of 100 kV. UV-vis spectroscopy was carried out using an Ocean optics spectrophotometer (HR4000Cg-UV-NIR) with 1 cm path length cuvettes in the wavelength range of 200-1000 nm. The electrochemical measurements were performed using a CHI760D electrochemical station. The XPS measurements were performed using a Thermo K-Alpha XPS instrument equipped with a monochromated Al K α radiation source with a 400 μm diameter spot size and 15 W X-ray gun power. The base pressure of the chamber was 2×10^{-8} mbar and the pressure of the chamber is maintained around 2.5×10^{-7} mbar during the experiment. The analyzer pass energy was set to 50 eV with an energy step size of 0.1 eV and a dwell time of 50 ms. The sample was flooded with a mix of low-energy electrons and an Ar-ion gun using the flood gun for charge compensation. The surface atoms of the sample were sputtered away with Ar+ ion gun with an energy of 500 eV for 60 s using a sputter gun and the residual surface was analyzed. All spectra were shift corrected using a C 1s (C-C peak) centered at 284.8 eV. X-ray diffraction (XRD) measurement was performed using Panalytical Empyrean with Cu K α radiation and 0.04 rad soller slits. The diffraction data was recorded from 2θ range of $30^{\circ}-90^{\circ}$ with the scan rate of 0.2°/min. The UPS spectra were collected by a UPS (Axis Ultra DLD, Kratos Analytical) instrument using He I radiation (energy = 21.21 eV). A Hitachi HD2700 aberrationcorrected scanning transmission electron microscope was used to acquire the high-angle annular dark-field (HAADF) STEM images and energy-dispersive X-ray (EDX) spectra. For all SERS measurements, a Renishaw RM1000 spectromicroscopy system was used with an air-cooled Ar laser (Mellos Griot) with a wavelength of 532 nm and a laser power of 12 mW. An Olympus LMPlanFI 20×/NA0.40 objective was used to focus the beam. The objective gave a spot size diameter of 2 μ m. The slit size was 10 μ m to minimize any distortion of the peaks. The WiRE software by Renishaw was used to set an acquisition time of 10 s per scan. A Coherent Libra-HE regeneratively amplified Ti:sapphire laser system with the fundamental output (3.5 mJ, 40 fs pulses centered at 808 nm) was used for experiments.

ASSOCIATED CONTENT

Supporting Information

The Supporting Information is available free of charge at https://pubs.acs.org/doi/10.1021/acsnano.1c02347.

Au and Pd contents of bimetallic nanoparticles, more HRTEM and STEM images, XRD data, UV—vis spectra, line profiles of bimetallic nanorods before and after fs laser irradiation, XPS and UPS data for bimetallic nanoparticles, photocurrent data using a laser source, PL measurements of Au nanospheres, FDTD simulations for individual and arrays of nanoparticles, and SERS data before and after PEC measurements (PDF)

AUTHOR INFORMATION

Corresponding Author

Mostafa A. El-Sayed — School of Chemistry and Biochemistry, Georgia Institute of Technology, Atlanta, Georgia 30332-0400, United States; orcid.org/0000-0002-7674-8424; Email: melsayed@gatech.edu

Authors

ı

Mohammadreza Nazemi – School of Chemistry and Biochemistry, Georgia Institute of Technology, Atlanta,

- Georgia 30332-0400, United States; o orcid.org/0000-0002-1735-9277
- Sajanlal R. Panikkanvalappil School of Chemistry and Biochemistry, Georgia Institute of Technology, Atlanta, Georgia 30332-0400, United States; Dana-Farber Cancer Institute, Harvard Medical School, Boston, Massachusetts 02210, United States; orcid.org/0000-0002-8337-9591
- Chih-Kai Liao Department of Biomedical Engineering and Chemical Engineering, University of Texas at San Antonio, San Antonio, Texas 78249, United States; orcid.org/0000-0002-0051-8884
- Mahmoud A. Mahmoud Department of Biomedical Engineering and Chemical Engineering, University of Texas at San Antonio, San Antonio, Texas 78249, United States; orcid.org/0000-0002-1986-1797

Complete contact information is available at: https://pubs.acs.org/10.1021/acsnano.1c02347

Notes

The authors declare no competing financial interest.

ACKNOWLEDGMENTS

This material is based upon work supported by the National Science Foundation under grant no. 1904351. This work was performed in part at the Georgia Tech Institute for Electronics and Nanotechnology, a member of the National Nanotechnology Coordinated Infrastructure (NNCI), which is supported by the National Science Foundation (grant ECCS-1542174). The authors acknowledge Professor Thomas Orlando for valuable conversations. The authors are also grateful to Dr. Z. Xu for his help with TA measurements.

REFERENCES

- (1) Grätzel, M. Solar Energy Conversion by Dye-Sensitized Photovoltaic Cells. *Inorg. Chem.* **2005**, *44*, 6841–6851.
- (2) Kamat, P. V. Meeting the Clean Energy Demand: Nanostructure Architectures for Solar Energy Conversion. *J. Phys. Chem. C* **2007**, 111, 2834–2860.
- (3) Lewis, N. S.; Nocera, D. G. Powering the Planet: Chemical Challenges in Solar Energy Utilization. *Proc. Natl. Acad. Sci. U. S. A.* **2006**, *103*, 15729–15735.
- (4) Huan, T. N.; Dalla Corte, D. A.; Lamaison, S.; Karapinar, D.; Lutz, L.; Menguy, N.; Foldyna, M.; Turren-Cruz, S.-H.; Hagfeldt, A.; Bella, F.; et al. Low-Cost High-Efficiency System for Solar-Driven Conversion of CO2 to Hydrocarbons. *Proc. Natl. Acad. Sci. U. S. A.* **2019**, *116*, 9735–9740.
- (5) Schreier, M.; Héroguel, F.; Steier, L.; Ahmad, S.; Luterbacher, J. S.; Mayer, M. T.; Luo, J.; Grätzel, M. Solar Conversion of CO2 to CO Using Earth-Abundant Electrocatalysts Prepared by Atomic Layer Modification of CuO. *Nature Energy* **2017**, *2*, 1–9.
- (6) Gurudayal, G.; Bullock, J.; Sranko, D. F.; Towle, C. M.; Lum, Y.; Hettick, M.; Scott, M. C.; Javey, A.; Ager, J. Efficient Solar-Driven Electrochemical CO2 Reduction to Hydrocarbons and Oxygenates. *Energy Environ. Sci.* **2017**, *10*, 2222–2230.
- (7) Ye, W.; Arif, M.; Fang, X.; Mushtaq, M. A.; Chen, X.; Yan, D. Efficient Photoelectrochemical Route for the Ambient Reduction of N2 to NH3 Based on Nanojunctions Assembled from MoS2 Nanosheets and TiO2. ACS Appl. Mater. Interfaces 2019, 11, 28809–28817.
- (8) Linic, S.; Christopher, P.; Ingram, D. B. Plasmonic-Metal Nanostructures for Efficient Conversion of Solar to Chemical Energy. *Nat. Mater.* **2011**, *10*, 911.
- (9) Clavero, C. Plasmon-Induced Hot-Electron Generation at Nanoparticle/Metal-Oxide Interfaces for Photovoltaic and Photocatalytic Devices. *Nat. Photonics* **2014**, *8*, 95.

- (10) Link, S.; El-Sayed, M. A. Spectral Properties and Relaxation Dynamics of Surface Plasmon Electronic Oscillations in Gold and Silver Nanodots and Nanorods. *J. Phys. Chem. B* **1999**, *103*, 8410–8426.
- (11) Jain, P. K.; Huang, X.; El-Sayed, I. H.; El-Sayed, M. A. Noble Metals on the Nanoscale: Optical and Photothermal Properties and Some Applications in Imaging, Sensing, Biology, and Medicine. *Acc. Chem. Res.* **2008**, *41*, 1578–1586.
- (12) Lakowicz, J. R. Radiative Decay Engineering: Biophysical and Biomedical Applications. *Anal. Biochem.* **2001**, 298, 1–24.
- (13) Fleischmann, M.; Hendra, P. J.; McQuillan, A. J. Raman Spectra of Pyridine Adsorbed at a Silver Electrode. *Chem. Phys. Lett.* **1974**, *26*, 163–166.
- (14) Albrecht, M. G.; Creighton, J. A. Anomalously Intense Raman Spectra of Pyridine at a Silver Electrode. *J. Am. Chem. Soc.* **1977**, *99*, 5215–5217.
- (15) Su, X.-R.; Zhang, W.; Zhou, L.; Peng, X.-N.; Wang, Q.-Q. Plasmon-Enhanced Förster Energy Transfer between Semiconductor Quantum Dots: Multipole Effects. *Opt. Express* **2010**, *18*, 6516–6521.
- (16) Gomez, D.; Vernon, K.; Mulvaney, P.; Davis, T. Surface Plasmon Mediated Strong Exciton—Photon Coupling in Semi-conductor Nanocrystals. *Nano Lett.* **2010**, *10*, 274—278.
- (17) Link, S.; El-Sayed, M. A. Shape and Size Dependence of Radiative, Non-Radiative and Photothermal Properties of Gold Nanocrystals. *Int. Rev. Phys. Chem.* **2000**, *19*, 409–453.
- (18) Mahmoud, M. A.; El-Sayed, M. A. Different Plasmon Sensing Behavior of Silver and Gold Nanorods. *J. Phys. Chem. Lett.* **2013**, *4*, 1541–1545.
- (19) Mahmoud, M. A.; O'Neil, D.; El-Sayed, M. A. Hollow and Solid Metallic Nanoparticles in Sensing and in Nanocatalysis. *Chem. Mater.* **2014**, *26*, 44–58.
- (20) Gupta, M. K.; König, T.; Near, R.; Nepal, D.; Drummy, L. F.; Biswas, S.; Naik, S.; Vaia, R. A.; El-Sayed, M. A.; Tsukruk, V. V. Surface Assembly and Plasmonic Properties in Strongly Coupled Segmented Gold Nanorods. *Small* **2013**, *9*, 2979–2990.
- (21) Lee, K.-S.; El-Sayed, M. A. Dependence of the Enhanced Optical Scattering Efficiency Relative to that of Absorption for Gold Metal Nanorods on Aspect Ratio, Size, End-Cap Shape, and Medium Refractive Index. J. Phys. Chem. B 2005, 109, 20331–20338.
- (22) Mahmoud, M. A.; Chamanzar, M.; Adibi, A.; El-Sayed, M. A. Effect of the Dielectric Constant of the Surrounding Medium and the Substrate on the Surface Plasmon Resonance Spectrum and Sensitivity Factors of Highly Symmetric Systems: Silver Nanocubes. *J. Am. Chem. Soc.* **2012**, *134*, 6434–6442.
- (23) Vanka, S.; Zhou, B.; Awni, R. A.; Song, Z.; Chowdhury, F. A.; Liu, X.; Hajibabaei, H.; Shi, W.; Xiao, Y.; Navid, I. A.; et al. InGaN/Si Double-Junction Photocathode for Unassisted Solar Water Splitting. *ACS Energy Letters* **2020**, *5*, 3741–3751.
- (24) Lee, S.; Hwang, H.; Lee, W.; Schebarchov, D.; Wy, Y.; Grand, J.; Auguie, B.; Wi, D. H.; Cortés, E.; Han, S. W. Core—Shell Bimetallic Nanoparticle Trimers for Efficient Light-to-Chemical Energy Conversion. ACS Energy Letters 2020, 5, 3881—3890.
- (25) Khan, R.; Naveen, M. H.; Abbas, M. A.; Lee, J.; Kim, H.; Bang, J. H. Photoelectrochemistry of Au Nanocluster-Sensitized TiO2: Intricacy Arising from the Light-Induced Transformation of Nanoclusters into Nanoparticles. ACS Energy Letters 2021, 6, 24–32.
- (26) Jang, Y. J.; Lindberg, A. E.; Lumley, M. A.; Choi, K.-S. Photoelectrochemical Nitrogen Reduction to Ammonia on Cupric and Cuprous Oxide Photocathodes. *ACS Energy Letters* **2020**, *5*, 1834–1839.
- (27) Hartland, G. V. Optical Studies of Dynamics in Noble Metal Nanostructures. *Chem. Rev.* **2011**, *111*, 3858–3887.
- (28) Nazemi, M.; El-Sayed, M. A. Plasmon-Enhanced Photo-(electro)chemical Nitrogen Fixation under Ambient Conditions Using Visible Light Responsive Hybrid Hollow Au-Ag2O Nanocages. Nano Energy 2019, 63, 103886.
- (29) Zhou, L.; Zhang, C.; McClain, M. J.; Manjavacas, A.; Krauter, C. M.; Tian, S.; Berg, F.; Everitt, H. O.; Carter, E. A.; Nordlander, P.;

- Halas, N. J. Aluminum Nanocrystals as a Plasmonic Photocatalyst for Hydrogen Dissociation. *Nano Lett.* **2016**, *16*, 1478–1484.
- (30) Yu, S.; Jain, P. K. Selective Branching of Plasmonic Photosynthesis into Hydrocarbon Production and Hydrogen Generation. ACS Energy Letters 2019, 4, 2295–2300.
- (31) Yu, S.; Jain, P. K. Plasmonic Photosynthesis of C1–C3 Hydrocarbons from Carbon Dioxide Assisted by an Ionic Liquid. *Nat. Commun.* **2019**, *10*, 1–7.
- (32) Zhou, L.; Swearer, D. F.; Zhang, C.; Robatjazi, H.; Zhao, H.; Henderson, L.; Dong, L.; Christopher, P.; Carter, E. A.; Nordlander, P.; Halas, N. J. Quantifying Hot Carrier and Thermal Contributions in Plasmonic Photocatalysis. *Science* **2018**, *362*, *69*–72.
- (33) Jain, P. K. Taking the Heat off of Plasmonic Chemistry. *J. Phys. Chem. C* **2019**, 123 (40), 24347–24351.
- (34) Brongersma, M. L.; Halas, N. J.; Nordlander, P. Plasmon-Induced Hot Carrier Science and Technology. *Nat. Nanotechnol.* **2015**, *10*, 25–34.
- (35) Aioub, M.; Panikkanvalappil, S. R.; El-Sayed, M. A. Platinum-Coated Gold Nanorods: Efficient Reactive Oxygen Scavengers that Prevent Oxidative Damage Toward Healthy, Untreated Cells during Plasmonic Photothermal Therapy. ACS Nano 2017, 11, 579—586.
- (36) Sun, L.; Zhang, Q.; Li, G. G.; Villarreal, E.; Fu, X.; Wang, H. Multifaceted Gold–Palladium Bimetallic Nanorods and Their Geometric, Compositional, and Catalytic Tunabilities. *ACS Nano* **2017**, 11, 3213–3228.
- (37) Swearer, D. F.; Zhao, H.; Zhou, L.; Zhang, C.; Robatjazi, H.; Martirez, J. M. P.; Krauter, C. M.; Yazdi, S.; McClain, M. J.; Ringe, E.; et al. Heterometallic Antenna—Reactor Complexes for Photocatalysis. *Proc. Natl. Acad. Sci. U. S. A.* **2016**, *113*, 8916—8920.
- (38) Aslam, U.; Rao, V. G.; Chavez, S.; Linic, S. Catalytic Conversion of Solar to Chemical Energy on Plasmonic Metal Nanostructures. *Nature Catalysis* **2018**, *1*, 656–665.
- (39) González-Rubio, G.; Díaz-Núñez, P.; Rivera, A.; Prada, A.; Tardajos, G.; González-Izquierdo, J.; Bañares, L.; Llombart, P.; Macdowell, L. G.; Palafox, M. A.; et al. Femtosecond Laser Reshaping Yields Gold Nanorods with Ultranarrow Surface Plasmon Resonances. *Science* 2017, 358, 640–644.
- (40) Grzelczak, M.; Perez-Juste, J.; García de Abajo, F. J.; Liz-Marzán, L. M. Optical Properties of Platinum-Coated Gold Nanorods. *J. Phys. Chem.* C **2007**, *111*, 6183–6188.
- (41) Grzelczak, M.; Pérez-Juste, J.; Rodríguez-González, B.; Liz-Marzán, L. M. Influence of Silver Ions on the Growth Mode of Platinum on Gold Nanorods. *J. Mater. Chem.* **2006**, *16*, 3946–3951.
- (42) Ye, W.; Kruger, K.; Sanchez-Iglesias, A.; Garcia, I.; Jia, X.; Sutter, J.; Celiksoy, S.; Foerster, B.; Liz-Marzan, L. M.; Ahijado-Guzman, R.; Sonnichsen, C. CTAB Stabilizes Silver on Gold Nanorods. *Chem. Mater.* **2020**, 32, 1650–1656.
- (43) Chi, Z.; Chen, H.; Chen, Z.; Zhao, Q.; Chen, H.; Weng, Y.-X. Ultrafast Energy Dissipation *via* Coupling with Internal and External Phonons in Two-Dimensional MoS2. *ACS Nano* **2018**, *12*, 8961–8969.
- (44) Huang, W.; Qian, W.; El-Sayed, M. A. Photothermal Reshaping of Prismatic Au Nanoparticles in Periodic Monolayer Arrays by Femtosecond Laser Pulses. *J. Appl. Phys.* **2005**, *98*, 114301.
- (45) Link, S.; Wang, Z. L.; El-Sayed, M. A. How Does a Gold Nanorod Melt? *J. Phys. Chem. B* **2000**, *104*, 7867–7870.
- (46) Link, S.; Burda, C.; Nikoobakht, B.; El-Sayed, M. A. Laser-Induced Shape Changes of Colloidal Gold Nanorods Using Femtosecond and Nanosecond Laser Pulses. *J. Phys. Chem. B* **2000**, 104, 6152–6163.
- (47) Hong, J. W.; Kim, D.; Lee, Y. W.; Kim, M.; Kang, S. W.; Han, S. W. Atomic-Distribution-Dependent Electrocatalytic Activity of Au–Pd Bimetallic Nanocrystals. *Angew. Chem., Int. Ed.* **2011**, *50*, 8876–8880
- (48) Zhang, D.; Gökce, B.; Barcikowski, S. Laser Synthesis and Processing of Colloids: Fundamentals and Applications. *Chem. Rev.* **2017**, *117*, 3990–4103.

- (49) Delfour, L.; Itina, T. E. Mechanisms of Ultrashort Laser-Induced Fragmentation of Metal Nanoparticles in Liquids: Numerical Insights. *J. Phys. Chem. C* **2015**, *119*, 13893–13900.
- (50) Yamada, K.; Miyajima, K.; Mafuné, F. Thermionic Emission of Electrons from Gold Nanoparticles by Nanosecond Pulse-Laser Excitation of Interband. *J. Phys. Chem. C* **2007**, *111*, 11246–11251.
- (51) Plech, A.; Kotaidis, V.; Lorenc, M.; Boneberg, J. Femtosecond Laser Near-Field Ablation from Gold Nanoparticles. *Nat. Phys.* **2006**, 2, 44–47.
- (52) Werner, D.; Furube, A.; Okamoto, T.; Hashimoto, S. Femtosecond Laser-Induced Size Reduction of Aqueous Gold Nanoparticles: *In Situ* and Pump—Probe Spectroscopy Investigations Revealing Coulomb Explosion. *J. Phys. Chem. C* **2011**, *115*, 8503—8512.
- (53) Werner, D.; Hashimoto, S. Improved Working Model for Interpreting the Excitation Wavelength- and Fluence-Dependent Response in Pulsed Laser-Induced Size Reduction of Aqueous Gold Nanoparticles. *J. Phys. Chem. C* **2011**, *115*, 5063–5072.
- (54) Huang, X.; El-Sayed, I. H.; Qian, W.; El-Sayed, M. A. Cancer Cell Imaging and Photothermal Therapy in the Near-Infrared Region by Using Gold Nanorods. *J. Am. Chem. Soc.* **2006**, *128*, 2115–2120.
- (55) Hirsch, L. R.; Stafford, R. J.; Bankson, J.; Sershen, S. R.; Rivera, B.; Price, R.; Hazle, J. D.; Halas, N. J.; West, J. L. Nanoshell-Mediated Near-Infrared Thermal Therapy of Tumors under Magnetic Resonance Guidance. *Proc. Natl. Acad. Sci. U. S. A.* **2003**, *100*, 13549–13554.
- (56) Nikoobakht, B.; El-Sayed, M. A. Preparation and Growth Mechanism of Gold Nanorods (NRs) Using Seed-Mediated Growth Method. *Chem. Mater.* **2003**, *15*, 1957–1962.
- (57) Nazemi, M.; Panikkanvalappil, S. R.; El-Sayed, M. A. Enhancing the Rate of Electrochemical Nitrogen Reduction Reaction for Ammonia Synthesis under Ambient Conditions Using Hollow Gold Nanocages. *Nano Energy* **2018**, *49*, 316–323.
- (58) Nahar, L.; Farghaly, A. A.; Esteves, R. J. A.; Arachchige, I. U. Shape Controlled Synthesis of Au/Ag/Pd Nanoalloys and Their Oxidation-Induced Self-Assembly into Electrocatalytically Active Aerogel Monoliths. *Chem. Mater.* **2017**, *29*, 7704–7715.
- (59) Cai, Y.-Y.; Liu, J. G.; Tauzin, L. J.; Huang, D.; Sung, E.; Zhang, H.; Joplin, A.; Chang, W.-S.; Nordlander, P.; Link, S. Photoluminescence of Gold Nanorods: Purcell Effect Enhanced Emission from Hot Carriers. *ACS Nano* **2018**, *12*, 976–985.
- (60) Joplin, A.; Hosseini Jebeli, S. A.; Sung, E.; Diemler, N.; Straney, P. J.; Yorulmaz, M.; Chang, W.-S.; Millstone, J. E.; Link, S. Correlated Absorption and Scattering Spectroscopy of Individual Platinum-Decorated Gold Nanorods Reveals Strong Excitation Enhancement in the Nonplasmonic Metal. ACS Nano 2017, 11, 12346–12357.
- (61) Kamat, P. V.; Flumiani, M.; Hartland, G. V. Picosecond Dynamics of Silver Nanoclusters. Photoejection of Electrons and Fragmentation. *J. Phys. Chem. B* **1998**, *102*, 3123–3128.
- (62) Nazemi, M.; Soule, L.; Liu, M.; El-Sayed, M. A. Ambient Ammonia Electrosynthesis from Nitrogen and Water by Incorporating Palladium in Bimetallic Gold—Silver Nanocages. *J. Electrochem. Soc.* **2020**, *167*, 054511.
- (63) Yang, J.; Guo, Y.; Jiang, R.; Qin, F.; Zhang, H.; Lu, W.; Wang, J.; Yu, J. C. High-Efficiency "Working-in-Tandem" Nitrogen Photofixation Achieved by Assembling Plasmonic Gold Nanocrystals on Ultrathin Titania Nanosheets. *J. Am. Chem. Soc.* **2018**, *140*, 8497—8508.
- (64) Minutella, E.; Schulz, F.; Lange, H. Excitation-Dependence of Plasmon-Induced Hot Electrons in Gold Nanoparticles. *J. Phys. Chem. Lett.* **2017**, *8*, 4925–4929.
- (65) Mahmoud, M. A.; Szymanski, P.; El-Sayed, M. A. Different Methods of Increasing the Mechanical Strength of Gold Nanocages. *J. Phys. Chem. Lett.* **2012**, *3*, 3527–3531.
- (66) Nazemi, M.; Ou, P.; Alabbady, A.; Soule, L.; Liu, A.; Song, J.; Sulchek, T. A.; Liu, M.; El-Sayed, M. A. Electrosynthesis of Ammonia Using Porous Bimetallic Pd—Ag Nanocatalysts in Liquid-and Gas-Phase Systems. ACS Catal. 2020, 10, 10197—10206.

- (67) Xie, H.; Geng, Q.; Zhu, X.; Luo, Y.; Chang, L.; Niu, X.; Shi, X.; Asiri, A. M.; Gao, S.; Wang, Z.; Sun, X. PdP2 Nanoparticles—Reduced Graphene Oxide for Electrocatalytic N2 Conversion to NH3 under Ambient Conditions. J. Mater. Chem. A 2019, 7, 24760—24764.
- (68) Deng, G.; Wang, T.; Alshehri, A. A.; Alzahrani, K. A.; Wang, Y.; Ye, H.; Luo, Y.; Sun, X. Improving the Electrocatalytic N2 Reduction Activity of Pd Nanoparticles through Surface Modification. *J. Mater. Chem. A* **2019**, *7*, 21674–21677.
- (69) Panikkanvalappil, S. R.; Hooshmand, N.; El-Sayed, M. A. Intracellular Assembly of Nuclear-Targeted Gold Nanosphere Enables Selective Plasmonic Photothermal Therapy of Cancer by Shifting Their Absorption Wavelength toward Near-Infrared Region. *Bioconjugate Chem.* 2017, 28, 2452–2460.
- (70) Zheng, Z.; Tachikawa, T.; Majima, T. Plasmon-Enhanced Formic Acid Dehydrogenation Using Anisotropic Pd–Au Nanorods Studied at the Single-Particle Level. *J. Am. Chem. Soc.* **2015**, *137*, 948–957.